ARTICLE

Check for updates

Facet-dependent electrooxidation of propylene into propylene oxide over Ag_3PO_4 crystals

Jingwen Ke[1,2], Jiankang Zhao[1,2], Mingfang Chi[1,2], Menglin Wang[1], Xiangdong Kong[1], Qixuan Chang[1], Weiran Zhou[1], Chengxuan Long[1], Jie Zeng [1] & Zhigang Geng [1✉]

The electrooxidation of propylene into propylene oxide under ambient conditions represents an attractive approach toward propylene oxide. However, this process suffers from a low yield rate over reported electrocatalysts. In this work, we develop an efficient electrocatalyst of Ag_3PO_4 for the electrooxidation of propylene into propylene oxide. The Ag_3PO_4 cubes with (100) facets exhibit the highest yield rate of 5.3 g_{PO} m^{-2} h^{-1} at 2.4 V versus reversible hydrogen electrode, which is 1.6 and 2.5 times higher than those over Ag_3PO_4 rhombic dodecahedra with (110) facets and tetrahedra with (111) facets, respectively. The theoretical calculations reveal that the largest polarization of propylene on Ag_3PO_4 (100) facets is beneficial to break the symmetric π bonding and facilitate the formation of C-O bond. Meanwhile, Ag_3PO_4(100) facets exhibit the lowest adsorption energies of $^*C_3H_6$ and $^*OH$, inducing the lowest energy barrier of the rate-determining step and thus accounting for the highest catalytic performance.

[1] Hefei National Laboratory for Physical Sciences at the Microscale, Key Laboratory of Strongly-Coupled Quantum Matter Physics of Chinese Academy of Sciences, Key Laboratory of Surface and Interface Chemistry and Energy Catalysis of Anhui Higher Education Institutes, Department of Chemical Physics, University of Science and Technology of China, Hefei, Anhui 230026, P. R. China. [2] These authors contributed equally: Jingwen Ke, Jiankang Zhao, Mingfang Chi. ✉email: gengzg@ustc.edu.cn

Propylene oxide (PO) is an important industrial intermediate that can be transformed into various commodity chemicals such as polymers, propylene glycol, polyurethane foams, propylene carbonate, and so on[1–3]. Common industrial methods of PO production include chlorohydrin process, Halcon process, directed oxidation process, and hydrogen peroxide-based process (HPPO)[4]. The chlorohydrin process requires abundant environmentally hazardous chlorine and produces a large amount of sludge[5]. The Halcon process involves autoxidation of ethylbenzene or isobutene to produce alkylhydroperoxide that acts as an oxidant to produce PO but accompanies with the substantial formation of peroxycarboxylate[6,7]. The directed oxidation process needs to be operated at high temperature, leading to the formation of byproducts such as acrolein and CO_2[8–10]. The HPPO has been restricted to manufacture PO from propylene due to the high cost and insufficient supply of H_2O_2[11–13]. Based on the aforementioned analysis, there is an urgent demand to develop an environmentally friendly, low-cost, and simple process to achieve a highly efficient synthesis of PO.

The electrooxidation of propylene into PO has attracted particular attention. This process utilizes sustainable and abundant water as an oxygen source under ambient conditions, with pure hydrogen generated on the counter electrode simultaneously[14–16]. Moreover, the mild reaction conditions require less handling and distribution infrastructure than those are necessary for PO production[17]. Currently, various catalysts have been applied to the electrooxidation of propylene[18–20]. For instance, Chorkendorff et al. prepared a Pd electrode that exhibited catalytic performance for the electrooxidation of propylene[21]. Since Pd favored the activation of C-H bond on allyl carbon, leading to the production of acrolein, the selectivity for PO was as low as 25%. Ag-based materials preferred to activate the C=C double bond rather than methyl hydrogen (α-H) in propylene, benefiting the formation of PO[8,9,22,23]. Holbrook et al. reported that PO was directly obtained via the electrooxidation of propylene on a silver electrode, but suffered from low activity (<0.01 g_{PO} m^{-2} h^{-1})[24]. For high yields of PO, it would be accessible if we modify Ag-based catalysts to enhance their activity.

A typical route to engineer the structures of Ag-based catalysts is based on regulating the exposed facets. The catalytic performance for the electrooxidation of propylene can be described by the adsorption energies of propylene ($E_{ads.Pr*}$) and oxygen species ($E_{ads.O*}$)[25–27]. Since $E_{ads.Pr*}$ and $E_{ads.O*}$ are sensitive to the facets, optimizing the catalytic performance requires the construction of uniform facets. Ideal facets should exhibit specific density of states (DOS) that properly overlap with the p orbitals of adsorbed propylene (Pr*) and oxygen species. Moreover, breaking the symmetric π bonding for the activation of C=C double bond demands the degree of propylene polarization that is also dependent on the facets. Therefore, fabricating uniform facets of Ag-based catalysts that are optimized by adjusting the DOS and propylene polarization serves as a promising way to promote the catalytic performance for the electrooxidation of propylene.

Herein, we developed highly efficient electrocatalysts of Ag_3PO_4 cubes that performed a high yield rate of PO production for the electrooxidation of propylene. Three types of Ag_3PO_4 crystals enclosed by (100), (110), and (111) facets were fabricated, including Ag_3PO_4 cubes, rhombic dodecahedra, and tetrahedra, respectively. During the electrooxidation of propylene, Ag_3PO_4 cubes exhibited the highest yield rate of 5.3 g_{PO} m^{-2} h^{-1} in 0.1 M phosphate buffer solution (PBS) at 2.4 V versus reversible hydrogen electrode (vs RHE), which was 1.6 and 2.5 times higher than those over Ag_3PO_4 rhombic dodecahedra and tetrahedra, respectively. Based on density functional theory (DFT) calculations, the formation of bidentate $CH_3CHCH_2OH^*$ (PrOH*) intermediate from Pr* and *OH was the rate-determining step

(RDS). The activation barrier for the formation of PrOH* on (100) facets was 1.27 eV, which was lower than those on (110) and (111) facets of Ag_3PO_4. The lowered $E_{ads.Pr*}$ and adsorption energies of OH$^-$ ($E_{ads.OH*}$) over Ag_3PO_4 cubes were favorable to the activation of propylene, resulting in the enhanced activity relative to Ag_3PO_4 rhombic dodecahedra and tetrahedra.

Results

Preparation and characterization of Ag_3PO_4 crystals. Typically, Ag_3PO_4 crystals with different exposed facets were prepared via solvent-phase synthesis under ambient pressure at room temperature[28,29]. As shown in the scanning electron microscopy (SEM) and transmission electron microscopy (TEM) images, Ag_3PO_4 crystals exhibited uniform morphologies of cubes, rhombic dodecahedra, and tetrahedra, respectively (Fig. 1a–c). The average edge length of Ag_3PO_4 crystals was around 750 nm (Fig. 1d–f). The SEM images and the corresponding energy-dispersive X-ray spectroscopy elemental mapping for Ag_3PO_4 crystals show the homogeneous distribution of Ag, P, and O elements throughout the whole structure (Supplementary Fig. 1). Figure 1g–i displays the selected area electron diffraction (SAED) patterns of Ag_3PO_4 crystals. The SAED pattern of an individual Ag_3PO_4 cube displayed (002) and (020) facets with a [100] zone axis. In addition, the SAED patterns of Ag_3PO_4 rhombic dodecahedron and Ag_3PO_4 tetrahedron were recorded along the [110] and [111] direction, implying that the exposed surface of Ag_3PO_4 rhombic dodecahedron and tetrahedron consisted of (110) and (111) facets, respectively[30]. To further confirm the dominated (100), (110), and (111) facets in the as-prepared Ag_3PO_4 cubes, rhombic dodecahedra, and tetrahedra, respectively, we conducted X-ray diffraction (XRD) measurements. As shown in Fig. 1j, all of the Ag_3PO_4 crystals displayed the characteristic peaks located at 20.9°, 29.7°, 33.3°, 36.6°, 42.5°, 47.8°, 52.7°, 55.0°, 57.3°, 61.6°, and 71.9°, which were attributed to the (110), (200), (210), (211), (220), (310), (222), (320), (321), (400), and (421) facets of the body-centered cubic structure of Ag_3PO_4 (JCPDS No. 06-0505)[31]. Based on the peak intensity of main diffractions of (200), (110), and (222) facets, the peak–intensity ratio of (200)/(110)/(222) for Ag_3PO_4 cubes, rhombic dodecahedra, and tetrahedra were calculated to be 1.85:0.99:1.00, 0.78:2.55:1.00, and 0.36:0.15:1.00, respectively. This result further indicates that the primarily exposed facets of Ag_3PO_4 cubes, rhombic dodecahedra, and tetrahedra are (100), (110), and (111) facets, respectively (Supplementary Table 1). To investigate the composition of Ag_3PO_4 crystals, we carried out X-ray photoelectron spectroscopy (XPS) measurements. Figure 1k shows the survey XPS spectra of Ag_3PO_4 crystals. The characteristic peaks at around 134, 285, 368, 374, 532, 574, and 604 eV were observed, which were attributed to P 2p, C 1s, Ag 3$d_{5/2}$, Ag 3$d_{3/2}$, O 1s, Ag 3$p_{3/2}$, and Ag 3$p_{1/2}$, respectively[32–34]. These results indicate that Ag_3PO_4 crystals possess the same chemical compositions.

Catalytic performance of Ag_3PO_4 crystals for the electrooxidation of propylene. The catalytic performance of Ag_3PO_4 crystals was evaluated in a three-compartment electrochemical cell equipped with gas diffusion electrode (GDE) for the electrooxidation of propylene (Supplementary Fig. 2). We conducted chronoamperometric measurements in 0.1 M PBS (pH = 7.0). After 1-h electrolysis, the catalytic products were determined to be PO, acetone, and acetic acid via ^{1}H nuclear magnetic resonance (^{1}H NMR) measurements (Supplementary Figs. 3 and 4). At all applied potentials, the faradaic efficiencies (FE) for acetone and acetic acid were lower than 5% (Supplementary Fig. 5). Almost 80% selectivity for PO among liquid products was obtained over Ag_3PO_4 cubes, with approximately 75% and 70%
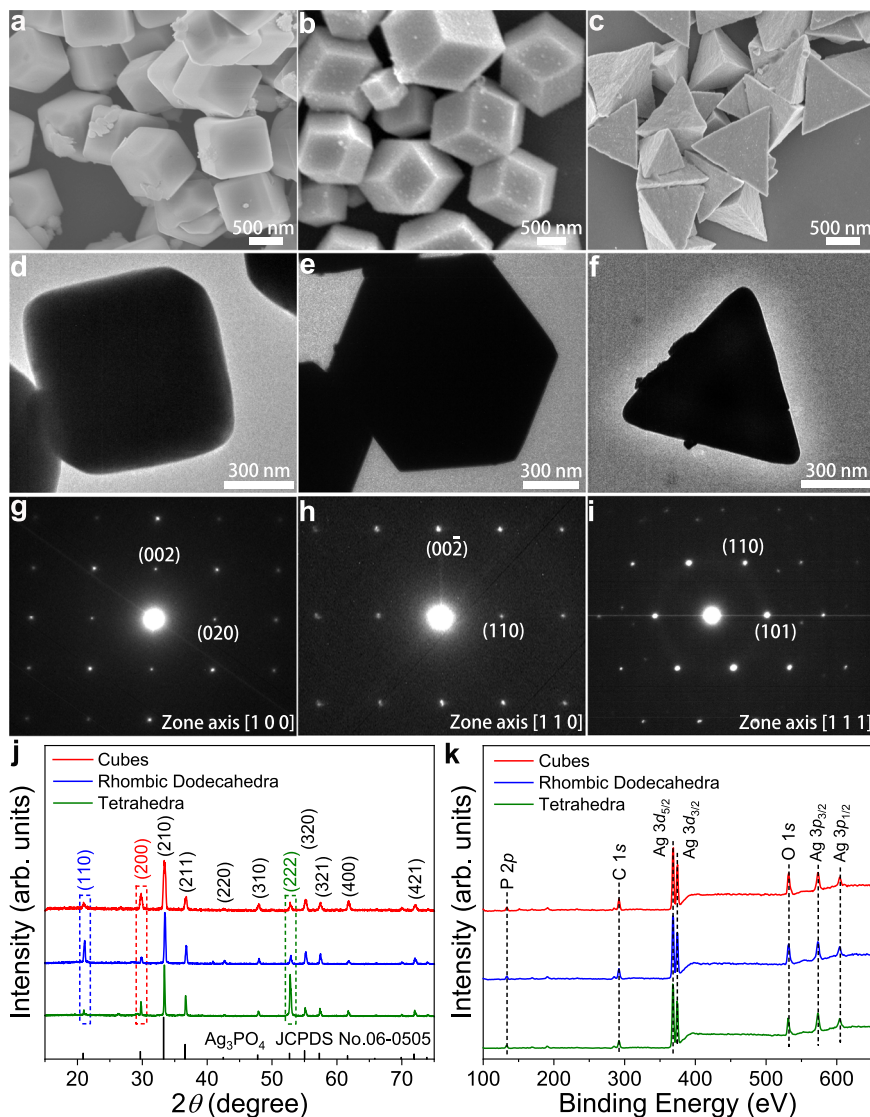
Fig. 1 Structural characterizations of Ag₃PO₄ crystals. a–c SEM images of Ag_3PO_4 cubes (**a**), rhombic dodecahedra (**b**), and tetrahedra (**c**). **d–f** TEM images of a Ag_3PO_4 cube (**d**), rhombic dodecahedron (**e**), and tetrahedron (**f**). **g–i** SAED images of a Ag_3PO_4 cube (**g**), rhombic dodecahedron (**h**), and tetrahedron (**i**). **j**, **k** XRD patterns (**j**) and survey XPS spectra (**k**) of Ag_3PO_4 cubes, rhombic dodecahedra, and tetrahedra.

selectivity for PO over Ag_3PO_4 rhombic dodecahedra and tetrahedra, respectively (Supplementary Fig. 6). As shown in Fig. 2a, Ag_3PO_4 cubes exhibited the highest FE for PO (FE_{PO}) among Ag_3PO_4 crystals at all applied potentials. Especially, at 2.2 V vs RHE, the FE_{PO} over Ag_3PO_4 cubes reached 18.7%, whereas the FE_{PO} over Ag_3PO_4 rhombic dodecahedra and tetrahedra were 15.9% and 13.1%, respectively. Figure 2b shows the partial current densities (j) of PO for Ag_3PO_4 crystals. The Ag_3PO_4 cubes exhibited higher partial j of PO (j_{PO}) with respect to the other two counterparts at all applied potentials. Notably, the j_{PO} over Ag_3PO_4 cubes reached the highest value of 0.49 mA cm^{-2} at 2.4 V vs RHE, whereas the j_{PO} over Ag_3PO_4 rhombic dodecahedra and tetrahedra were 0.31 and 0.19 mA cm^{-2}, correspondingly. The Ag_3PO_4 cubes exhibited the highest yield rate of 5.3 g$_{PO}$ m^{-2} h^{-1} at 2.4 V vs RHE, which was 1.6 and 2.5 times higher than those over Ag_3PO_4 rhombic dodecahedra (3.4 g$_{PO}$ m^{-2} h^{-1}) and Ag_3PO_4 tetrahedra (2.1 g$_{PO}$ m^{-2} h^{-1}) (Fig. 2c). Notably, Ag_3PO_4 cubes exhibited a record-high yield rate for PO production among previously reported electrocatalysts for the electrooxidation of propylene (Supplementary Table 2). To explore the intrinsic activity of Ag_3PO_4 crystals, we normalized the j_{PO} by

electrochemical surface area (ECSA). The ECSAs of Ag_3PO_4 crystals were determined by measuring double-layer capacitance (C_{dl}) using cyclic voltammetry (CV) measurements with different scan rates (Supplementary Fig. 7 and Supplementary Table 3). Figure 2d shows the ECSAs-normalized j_{PO}. At all applied potentials, the ECSA-normalized j_{PO} over Ag_3PO_4 cubes were always the highest among Ag_3PO_4 crystals. The highest ECSA-normalized j_{PO} of 0.16 mA cm^{-2} was obtained over Ag_3PO_4 cubes at 2.4 V vs RHE, which was 2.3 and 5.3 times as high as those over Ag_3PO_4 rhombic dodecahedra (0.07 mA cm^{-2}) and Ag_3PO_4 tetrahedra (0.03 mA cm^{-2}), respectively. Meanwhile, normalized by the ECSA, the commercial Ag_3PO_4 exhibited a low ECSA-normalized j_{PO} of 0.01 mA cm^{-2} at 2.4 V vs RHE, which was lower than those of the three types of Ag_3PO_4 crystals (Supplementary Fig. 8). Accordingly, Ag_3PO_4 cubes with exposed (100) facets possessed the highest intrinsic activity for the electrooxidation of propylene.

To investigate the structural stability of Ag_3PO_4 cubes during the electrooxidation of propylene, we conducted the in situ X-ray absorption near-edge spectroscopy (XANES) measurements. Based on in situ Ag K-edge XANES profiles, Ag_3PO_4 cubes at
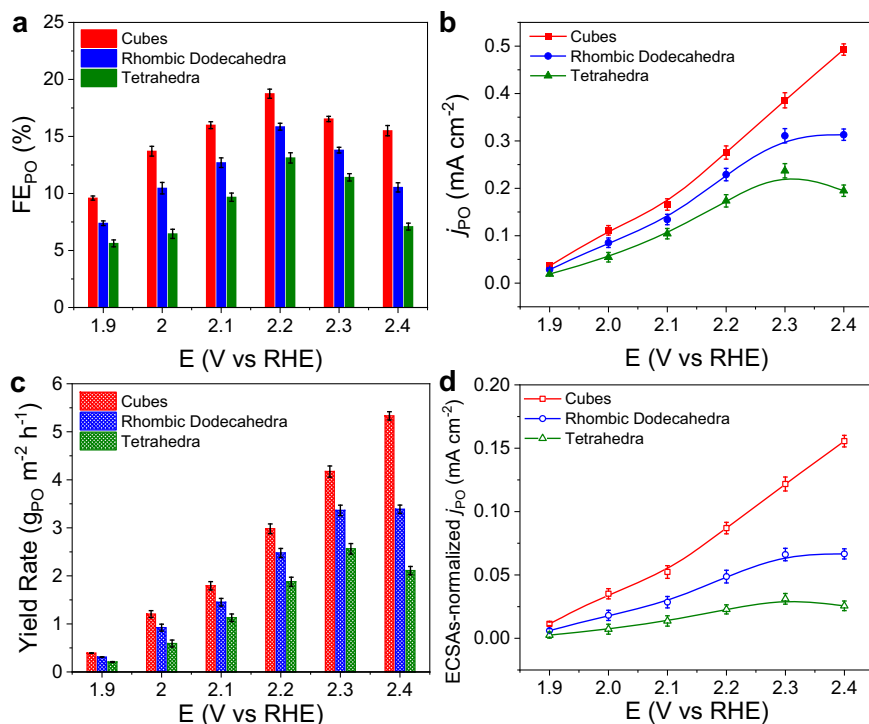
Fig. 2 Catalytic performance of Ag$_3$PO$_4$ crystals for the electrooxidation of propylene. a–d FE$_{PO}$ (**a**), j_{PO} (**b**), yield rates of PO (**c**), and ECSAs-normalized j_{PO} (**d**) over Ag$_3$PO$_4$ crystals. The error bars represent the standard deviations for the three independent measurements.

2.2 and 2.5 V vs RHE exhibited an energy absorption edge profile in a range from 25,450 to 25,650 eV similar to that of pristine Ag$_3$PO$_4$ cubes (Supplementary Fig. 9). The durability tests of Ag$_3$PO$_4$ cubes were proceeded via chronoamperometric measurement for 10 rounds of successive reactions at 2.2 V vs RHE. The FE$_{PO}$ over Ag$_3$PO$_4$ cubes remained above 17.0% (Supplementary Fig. 10). After durability tests, the SEM images and XRD patterns revealed that the morphology and phase of Ag$_3$PO$_4$ cubes were perfectly preserved (Supplementary Figs. 11 and 12). The contents of the Ag in the electrolytes and Ag$_3$PO$_4$ cubes were also determined via inductively coupled plasma atomic emission spectroscopy and X-ray Fluorescence Spectrometer (Supplementary Tables 4 and 5), respectively. These results suggest that Ag$_3$PO$_4$ cubes are stable during the electrooxidation of propylene. As shown in Supplementary Fig. 13, the contact angle of electrolyte on the GDE of Ag$_3$PO$_4$ cubes was reduced from 129.9° to 63.4° after ten successive reaction rounds. The transformation of the GDE from hydrophobicity to hydrophilicity would cause the penetration of electrolyte and hinder the diffusion of propylene, resulting in the decreased FE$_{PO}$.

Reaction paths over Ag$_3$PO$_4$ crystals. To provide a theoretical insight into the reaction mechanism, we carried out DFT calculations by adopting (100), (110), and (111) facets of Ag$_3$PO$_4$ cubes, Ag$_3$PO$_4$ rhombic dodecahedra, and Ag$_3$PO$_4$ tetrahedra as model slabs, respectively (Supplementary Fig. 14). The most stable (100), (110), and (111) facets of Ag$_3$PO$_4$ crystals possessed different Ag-terminated surfaces via calculating the minimal total energy (Supplementary Table 6). Figure 3a and Supplementary Fig. 15 show the process of electrooxidation of propylene. H$_2$O is adsorbed and dissociated into *OH on Ag sites. Afterwards, we considered two reaction pathways classified by adsorbed oxygen species of *OH (OH-correlated pathway) or *O (O-correlated pathway). For OH-correlated pathway, *OH species directly reacts with Pr* to produce a bidentate PrOH* intermediate. Subsequently, the O-H bond in PrOH* is further dissociated to CH$_3$CHCH$_2$O* (PrO*) intermediate,

which is an oxametallacycle intermediate during vapor-phase epoxidation of olefin[35,36]. With regard to O-correlated pathway, *OH is further dehydrogenated to *O and couples with Pr* to generate PrO*. For the generation of *O, there are two pathways that have been considered[37,38]. As shown in Supplementary Table 7, the change of Gibbs free energy (ΔG) for direct dehydrogenation of *OH was lower than that for the disproportionation of *OH over the (100), (110), and (111) facets of Ag$_3$PO$_4$, respectively. As such, all of the *O are generated from direct dehydrogenation of *OH over the three types of Ag$_3$PO$_4$ facets. Finally, PrO* is transformed to adsorbed PO (PO*) before desorption. The apparent energy barrier is defined as the energy difference between the initial state and the transition state (TS) with the highest energy. As shown in Fig. 3b–d, the apparent energy barriers (initial state→TS1) of OH-correlated pathway are lower than those (initial state→TS3) of O-correlated pathway for each facet of Ag$_3$PO$_4$ crystals. The electrooxidation of propylene could also undergo the dehydrogenation pathway, but the product would be allyl alcohol, acrolein, and acrylic acid rather than PO according to the previous literatures[21,23]. In addition, the energy barrier for the dehydrogenation of propylene is 1.50 eV on (100) facets of Ag$_3$PO$_4$, which is higher than that (1.27 eV) for the OH-correlated pathway (Supplementary Fig. 16). To further confirm the OH-correlated pathway with the formation of PrOH* intermediate, we conducted the in situ attenuated total reflection Fourier-transform infrared spectroscopy (ATR-FTIRS) experiment. Supplementary Fig. 17 shows the in situ ATR-FTIRS spectra over the Ag$_3$PO$_4$ cubes with the applied potentials ranging from 1.0 to 2.6 V vs RHE. The peaks at 1473, 1442, and 1417 cm^{-1} were assigned to the gaseous propylene[39], which exhibited a decreasing trend as the applied potentials scanning from 1.0 to 2.6 V vs RHE. When the applied potentials were increased, the intensities of the two peaks located at 1541 and 1457 cm^{-1} were also gradually increased. The two characteristic peaks were ascribed to the vibrations of the -C=C- and -CH$_3$ in Pr*[40,41], respectively, which was a significant intermediate for the formation of PrOH*. Especially, a small peak at 1434 cm^{-1} was observed at potentials higher than 1.6 V vs RHE. The
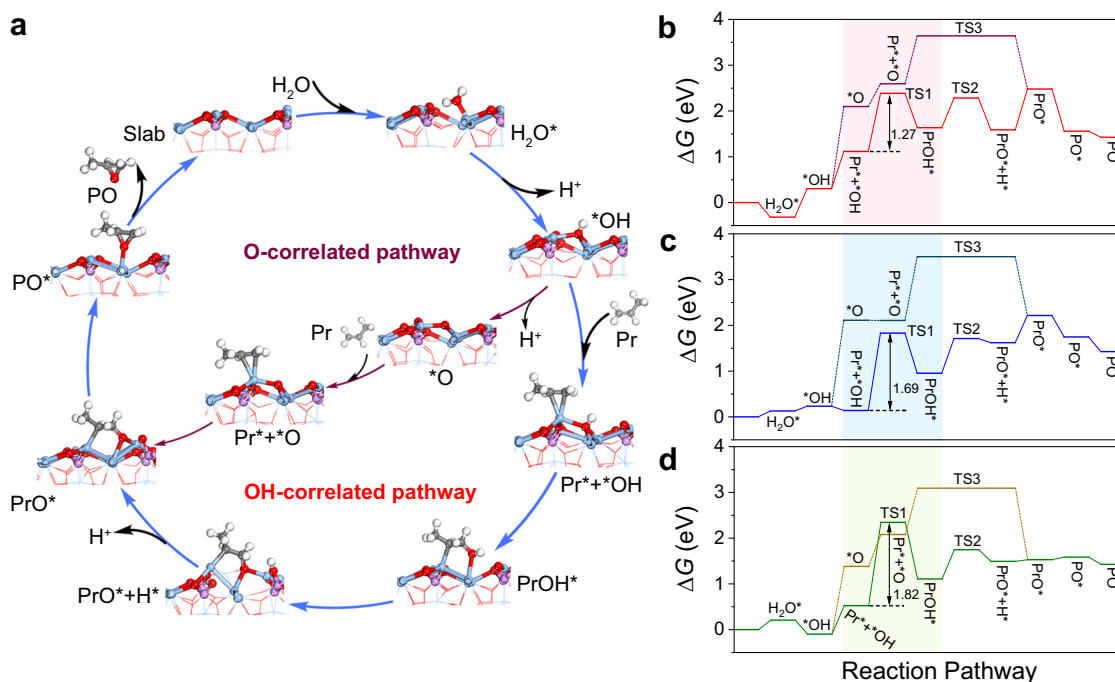
Fig. 3 Reaction paths over Ag$_3$PO$_4$ crystals. a Scheme of the two reaction pathways on (100) facets of Ag$_3$PO$_4$. The gray, white, blue, red, and light pink spheres represent C, H, Ag, O, and P atoms, respectively. **b** Free energy diagram of electrooxidation of propylene with OH-correlated pathway (red) and O-correlated pathway (wine) on (100) facets of Ag$_3$PO$_4$. **c** Free energy diagram of electrooxidation of propylene with OH-correlated pathway (blue) and O-correlated pathway (navy) on (110) facets of Ag$_3$PO$_4$. **d** Free energy diagram of electrooxidation of propylene with OH-correlated pathway (green) and O-correlated pathway (chartreuse) on (111) facets of Ag$_3$PO$_4$. * represents the adsorption site.

characteristic peak was assigned to the vibration of -CH$_2$- in PrOH* intermediate, which was consistent with the calculated peak position of PrOH* species (Supplementary Fig. 17, insert). As such, the electrooxidation of propylene over Ag$_3$PO$_4$ crystals undergoes the OH-correlated pathway rather than the O-correlated and dehydrogenation pathway.

Mechanisms of facet effect. We measured the apparent activation energies and reaction orders over three types of Ag$_3$PO$_4$ catalysts. As shown in Supplementary Fig. 18a, the Arrhenius plots of the three types of Ag$_3$PO$_4$ crystals were obtained. The apparent activation energy of Ag$_3$PO$_4$ cubes was 8.1 kJ mol^{-1}, which was lower than those of Ag$_3$PO$_4$ rhombic dodecahedra (10.6 kJ mol^{-1}) and Ag$_3$PO$_4$ tetrahedra (15.1 kJ mol^{-1}). The reaction order for the electrooxidation of propylene was estimated by plotting the ECSA-normalized j_{PO} at 2.2 V vs RHE against the partial pressures of propylene (Supplementary Fig. 18b). For Ag$_3$PO$_4$ cubes, the reaction order was 0.00, whereas the reaction orders of Ag$_3$PO$_4$ rhombic dodecahedra and tetrahedra were 0.35 and 0.44, respectively. These results illustrate that the Ag$_3$PO$_4$ cubes with exposed (100) facets promote the propylene activation, resulting in the high catalytic activity for the electrooxidation of propylene into PO. We also investigated the dependence of RDS on different facets of Ag$_3$PO$_4$ along the OH-correlated pathway. The formation of PrOH* exhibited the highest reaction energy barrier among all the steps independent of facets of Ag$_3$PO$_4$ crystals. Thus, the formation of PrOH* serves as the RDS during the electrooxidation of propylene. Specially, the energy barriers of the RDS on (110) and (111) facets of Ag$_3$PO$_4$ were 1.69 and 1.82 eV, respectively, both higher than that (1.27 eV) on (100) facets of Ag$_3$PO$_4$. As such, Ag$_3$PO$_4$ cubes favor the activation of propylene relative to Ag$_3$PO$_4$ rhombic dodecahedra and Ag$_3$PO$_4$ tetrahedra (Fig. 3b–d). To rationalize the facet-dependent energy barriers of RDS, we analyzed the adsorption configuration of Pr* and OH* on Ag$_3$PO$_4$ by comparing the distance of C-O between the C in CH$_2$ for

Pr* and O for *OH during the RDS. As shown in Supplementary Fig. 19, the (100) facets of Ag$_3$PO$_4$ exhibited the shortest C-O distance of 1.91 Å in the TS1. The shortened C-O distance benefits the formation of C-O bond, corresponding to the lowered barrier of RDS. Considering that the RDS involved the coupling of Pr* (C) and *OH (O), we further calculated the $E_{ads.Pr*}$ and $E_{ads.*OH}$[42,43]. As shown in Fig. 4a, the $E_{ads.Pr*}$ and $E_{ads.*OH}$ on (100) facets of Ag$_3$PO$_4$ are the lowest among the three types of facets. As such, the energy barrier of the RDS has a positive correlation with the absolute value of $E_{ads.Pr*}$ and $E_{ads.*OH}$.

To further probe the structure–activity relationship during electrooxidation of propylene over Ag$_3$PO$_4$, we also analyzed the electronic properties of different Ag sites. Both the bond energies of Ag-C and Ag-O that influenced the $E_{ads.Pr*}$ and $E_{ads.*OH}$, respectively, were analyzed based on the DOS. Figure 4b shows the projected DOS of these surface Ag atoms on (100), (110), and (111) facets of Ag$_3$PO$_4$. The d-band center of Ag sites on (100) facets shifts away from the Fermi level compared with those on (110) and (111) facets of Ag$_3$PO$_4$, which exhibits the least overlap with the p orbitals of C in Pr* and O in *OH. These results reveal that Ag sites on (100) facets of Ag$_3$PO$_4$ display the lowest binding energies of both Pr* and *OH[44]. In addition, from the Bader charge analysis, the secondary carbon (CH$_2$) and tertiary carbon (CH) are –0.19 |e| and –0.09 |e| charged, respectively, for propylene adsorption on (100) facets of Ag$_3$PO$_4$ (Supplementary Fig. 20). The difference between these two C atoms is 0.1 |e| whereas the differences on (110) and (111) facets of Ag$_3$PO$_4$ are 0.07 |e| and 0.01 |e|, respectively. In this case, the polarization of propylene on (100) facets of Ag$_3$PO$_4$ was the largest among all the facets. The polarization of propylene and negative secondary carbon atoms broke the symmetric π bonding and facilitated the formation of C-O bond.

To gain insight into the facet-dependent binding energies of *OH and Pr*, we conducted the OH$^-$ and propylene stripping experiments[21,45–47]. As shown in Fig. 4c, the reduction peaks of
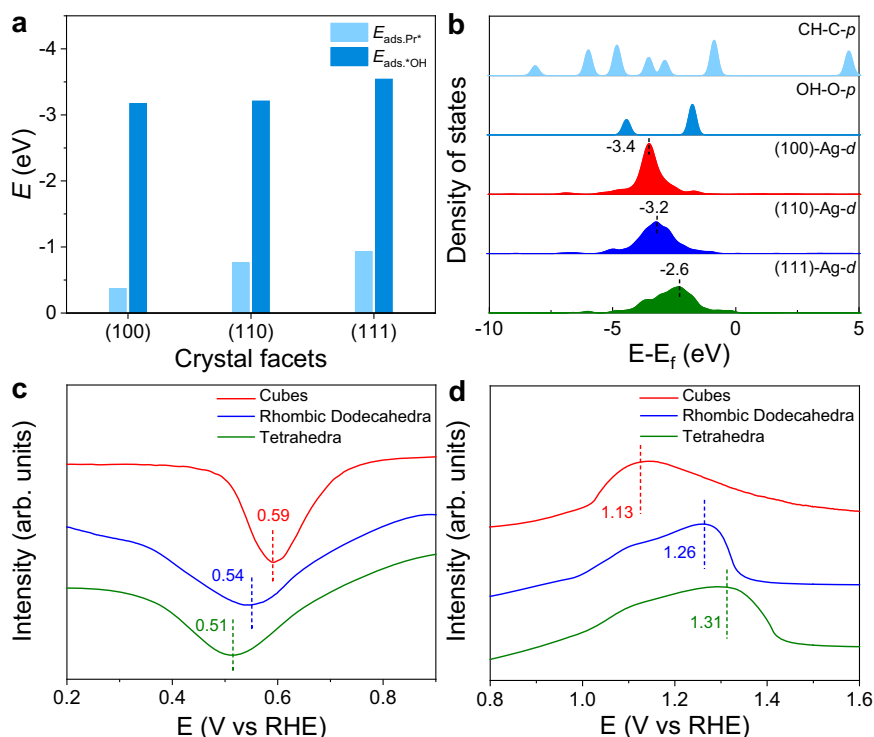
Fig. 4 Mechanisms of facet effect. a $E_{ads.Pr*}$ and $E_{ads.*OH}$ over the three types of Ag_3PO_4 facets. **b** Projected DOS plots of d orbitals of Ag over the three types of Ag_3PO_4 facets with p orbitals of C in Pr^* and O in $^*OH$. The d-band center was marked via short dash. **c, d** The single reduction of linear sweep voltammetric curves (**c**) and propylene stripping voltammograms (**d**) with the scan rate of 100 mV s^{-1} over Ag_3PO_4 crystals.

surface hydroxyl intermediates shifted from 0.59 V vs RHE (Ag_3PO_4 cubes) to 0.54 V (Ag_3PO_4 rhombic dodecahedra) and 0.51 V vs RHE (Ag_3PO_4 tetrahedra), respectively. These results suggest that the binding energy of $^*OH$ on Ag_3PO_4 cubes is the lowest among all the samples. Figure 4d shows the propylene stripping profiles over Ag_3PO_4 crystals. A broad peak at around 1.13 V vs RHE was observed over Ag_3PO_4 cubes. Meanwhile, the stripping peaks of propylene over Ag_3PO_4 rhombic dodecahedra and tetrahedra were located at around 1.26 and 1.31 V vs RHE. The positive shift of the peak potential manifested that the adsorbed strength of Pr^* over Ag_3PO_4 cubes was lower than those over Ag_3PO_4 rhombic dodecahedra and Ag_3PO_4 tetrahedra. Both DFT calculations and experiments proved that $E_{ads.Pr*}$ and $E_{ads.*OH}$ over Ag_3PO_4 cubes were the lowest, which was consistent with the highest activity for the electrooxidation of propylene.

Discussion

We achieved highly efficient electrocatalysts of Ag_3PO_4 cubes which performed a high yield rate (5.3 g_{PO} m^{-2} h^{-1}) of PO production for the electrooxidation of propylene. Moreover, we demonstrated the facet effect from two aspects. On the one hand, the DOS of (100) facets on Ag_3PO_4 exhibited the least overlap with the p orbitals of C in Pr^* and O in $^*OH$, thus displaying the lowest $E_{ads.Pr*}$ and $E_{ads.*OH}$. The weakened adsorption of Pr^* and $^*OH$ lowered the energy barrier of $PrOH^*$ formation that was determined as the RDS, accounting for the enhanced activity. On the other hand, the polarization of propylene on (100) facets of Ag_3PO_4 was the largest among all the facets from the Bader charge analysis, which was conducive to breaking the symmetric π bonding and facilitating the formation of C–O bond. Our work not only offers an effective catalyst for the electrooxidation of propylene but also advances the understanding of the facet effect on catalytic performance.

Methods

Chemicals and materials. Ammonium nitrate (NH_4NO_3, 99%), silver nitrate ($AgNO_3$, 99.8%), sodium hydroxide (NaOH, 99%), potassium hydrogen phosphate (K_2HPO_4, 99.5%), ethanol (EtOH, 99.8%) were all purchased from Sinopharm Chemical Reagent Co. Ltd. (Shanghai, China). 1-Propanesulfonic acid 3-(tri-methylsilyl) sodium salt (DSS), Dimethyl Sulfoxide-d6 (99.9 atom % D, contains 0.03% v/v TMS), Nafion solution (5 wt%) and Nafion 115 film were purchased from Sigma-Aldrich. PO (99.5%), acetone (99.5%), acetic acid (99.5%), and commercial Ag_3PO_4 were purchased from Aladdin Co. Ltd. (Shanghai, China). The deionized (DI) water with a resistivity of 18.2 MΩ cm was provided by a Millipore Milli-Q grade. All of the chemicals were used without any further purification.

Synthesis of Ag_3PO_4 cubes. In a typical procedure, 89.2 mL of DI water was added to the beaker, then 1 mL of NH_4NO_3 solution (0.4 M), 1.8 mL of NaOH solution (0.2 M), and 4 mL of $AgNO_3$ solution (0.05 M) were added to the beaker sequentially. The solution was stirred vigorously for 10 min to prepare the $[Ag(NH_3)_2]^+$ complex. Finally, 4 mL of K_2HPO_4 solution (0.1 M) was added to the complex and stirred for 5 min. After the solution color turned from colorless to light yellow, Ag_3PO_4 cubes were obtained. The as-obtained precipitate was separated by centrifugation and washed subsequently with DI water three times.

Synthesis of Ag_3PO_4 rhombic dodecahedra. Except for the feeding ratio of the reactants, the synthetic method of rhombic dodecahedra was similar to that of cubes. Specifically, 89.2 mL of DI water was replaced by 84.2 mL of DI water. 1 mL of NH_4NO_3 solution (0.4 M) was substituted by 6 mL of NH_4NO_3 solution (0.4 M). The other steps were the same as those of cubes.

Synthesis of Ag_3PO_4 tetrahedra. Three mmol of $AgNO_3$ was dissolved in 30 mL of ethanol under rapid stirring for the formation of $AgNO_3$-ethanol solution. Simultaneously, 5 mL of H_3PO_4 was mixed with 30 mL of ethanol for the formation of H_3PO_4-ethanol solution. Then, the $AgNO_3$-ethanol solution was added dropwise to the H_3PO_4-ethanol solution, until the mixture turned slightly cloudy. Finally, the mixture was added back into the $AgNO_3$-ethanol solution. After 1-h stirring, the solution turned bright green. The as-obtained precipitate was separated by centrifugation and washed subsequently with ethanol three times.

Preparation of working electrodes. For all Ag_3PO_4 crystals, the as-prepared sample and Nafion solution were ultrasonically suspended in ethanol and uniformly spread on carbon papers with a loading amount of 2.5 mg cm^{-2}.

Electrochemical measurements. For the electrooxidation of propylene, the electrochemical measurements were carried out in a three-compartment electrochemical cell equipped with a GDE. Graphite rod and Ag/AgCl electrodes were used as the counter electrode and reference electrode, respectively. The potentials were controlled by an Autolab potentiostat/galvanostat (CHI 660E). All potentials were measured against the Ag/AgCl reference electrode and converted to the RHE reference scale on account of the equation:

$$E(\text{vs RHE}) = E(\text{vs Ag/AgCl}) + 0.21\text{V} + 0.0591 \times \text{pH} \quad (1)$$

After propylene was purged into the gas cavity for 300 s to remove the residual air, chronoamperometric electrolysis was performed at each potential for 1 h. The liquid products in the electrolyte were quantified via ^{1}H NMR analysis. The FE$_{PO}$ was calculated at a given potential as follows:

$$\text{FE} = c \times V \times N \times F/Q \quad (2)$$

where c represents the concentration of product for PO, V represents the volume of the electrolyte, N represents the number of electrons transferred for product formation, which is 2 for PO, F is the Faraday constant, and Q represents the quantity of electric charge integrated by i–t curve.

The CV measurements were conducted in 0.1 M PBS solution using a three-electrode cell equipped with an Ag/AgCl reference electrode and a graphite counter electrode. 10 mg of the catalyst was dispersed in a mixture of 950-μL ethanol and 50-μL Nafion solution under ultrasonic stirring to form a homogenous ink. Ten microliter of the ink was then dropped onto a glassy carbon disk electrode by a micropipette to form a catalyst layer. CVs of Ag$_3$PO$_4$ crystals were conducted with various scan rates (10, 20, 30, 40, 50, 60, 70, 80, 90, and 100 mV s^{-1}) under argon atmosphere to obtain the double-layer capacitance (C_{dl}). The C_{dl} was estimated by plotting the Δj (j_a–j_c) in the middle of the scan range against the scan rates, where j_a and j_c were the anodic and cathodic current density, respectively. The linear slope was equivalent to twice of the C_{dl}. The ECSAs was calculated by the following equation:

$$\text{ECSAs} = R_f S \quad (3)$$

where R_f represented the roughness factor of Ag$_3$PO$_4$ surface and S represented the surface area of carbon paper electrode (1 cm^2 in this case). Based on the C_{dl} of a smooth oxide surface (60 μF cm^{-2} for Ag$_3$PO$_4$ surface[48]), R_f was calculated according to the relation $R_f = C_{dl}/60$.

Instrumentations. XRD patterns were recorded by using a Philips X'Pert Pro Super diffractometer with Cu-$K\alpha$ radiation ($\lambda = 1.54178$ Å). XPS measurements were performed on a VG ESCALAB MK II X-ray photoelectron spectrometer with an exciting source of Al $K\alpha = 1486.6$ eV. The liquid products were examined on a Varian 400 MHz NMR spectrometer (Bruker AVANCE AV III 400). SEM images were taken using a Hitachi SU8220 scanning electron microscope. TEM images were taken using a Hitachi H-7650 transmission electron microscope at an acceleration voltage of 100 kV. SAED were carried out on a JEOL ARM-200F field-emission transmission electron microscope operating at an accelerating voltage of 200 kV using Cu-based TEM grids. Inductively coupled plasma atomic emission spectroscopy (Atomscan Advantage, Thermo Jarrell Ash, USA) was conducted to determine the concentration of Ag species. X-Ray Fluorescence Spectrometer (XRF-1800, SHIMADZU) was used to qualify the molar ratio of Ag to P for the GDE of Ag$_3$PO$_4$ cubes. The in situ ATR-FTIRS measurements were carried out on a Nicolet iS50 with a wavenumber resolution of 4 cm^{-1} at room temperature.

In situ XANES measurements. In situ XANES experiments were carried out at BL14W1 beamline of Shanghai Synchrotron Radiation Facility. The XANES spectra of Ag K-edge ($E_0 = 25514$ eV) were operated at 3.5 GeV under "top-up" mode with a constant current of 260 mA. The in situ XANES data were recorded under fluorescence mode with a H-cell. The electrolyte was propylene-saturated 0.1 M PBS (pH = 7), while Ag/AgCl and a graphite rod acted as a reference and counter electrodes, respectively. The working electrode was prepared with a loading amount of 2.5 mg cm^{-2} for Ag$_3$PO$_4$ cubes. The energy was calibrated accordingly to the absorption edge of pure Ag foil. For the X-ray absorption near-edge structure part, the experimental absorption coefficients as a function of energies μ(E) were processed by background subtraction and normalization procedures, which were reported as "normalized absorption".

Computational methods. The Vienna ab initio Simulation Package was implemented in the DFT calculation in this work[49]. The projector augmented wave method and Perdew–Burke–Ernzerhof generalized gradient approximation method were used to describe the inner cores and the contributions of exchange-correlation functional, respectively[50,51]. The total energy calculations were performed using a $3 \times 3 \times 1$ grid and a plane wave cut-off energy of 400 eV. The (100) facet of Ag$_3$PO$_4$ contained three unit layers (12 atomic layers) with a supercell formula of Ag$_{36}$P$_{12}$O$_{48}$. The (110) facet of Ag$_3$PO$_4$ contained two layers with a supercell formula of Ag$_{24}$P$_8$O$_{32}$. The (111) facet of Ag$_3$PO$_4$ contained three Ag$_3$PO$_4$ layers with a supercell formula of Ag$_{36}$P$_{12}$O$_{48}$. A vacuum space of 12 Å was added in Z-direction to avoid the interactions between each slab. Atoms in the bottom Ag$_3$PO$_4$ layer were fixed and all other atoms including adsorbates were allowed to relax until the force on each ion was smaller than 0.02 eV/Å.

The Gibbs free energy changes (ΔG) for the elementary steps in the proposed mechanism are calculated as follows:

$$\Delta G = \Delta E_{DFT} + \Delta\text{ZPE} - T\Delta S \quad (4)$$

Here, ΔE_{DFT} is the change of energies of the optimized structures from DFT calculations. ΔZPE is the zero-point energy difference by analyzing the frequencies. ΔS is the entropy of each intermediate. It is assumed that $S = 0$ for all the adsorbed species. TSs of key elementary steps were searched using the climbing image nudged elastic band method[52]. All TSs were confirmed as true saddle points with a single imaginary frequency mode along the reaction coordinate. According to the model of computational hydrogen electrode, at standard conditions, the free energy change of the surface deprotonation process is equivalent to the hydrogen production, namely $^*\text{H} + \text{e}^- = 1/2 \, \text{H}_2$[53]. The adsorption energy (E_{ads}) is defined as follows:

$$E_{ads} = E_{adsorb/surf} - E_{surf} - E_{adsorb} \quad (5)$$

where $E_{adsorb/surf}$, E_{surf}, and E_{adsorb} represent the total energies of the slab with adsorbate(s), the clean slab, and the isolated adsorbate, respectively.

Data availability

All the data supporting this study are available in the paper and Supplementary Information. Source Data are provided with this paper.

Code availability

The codes and simulation files that support the plots and data analysis within this paper are available from the corresponding author upon reasonable request.

References

1. Teržan, J., Huš, M., Likozar, B. & Djinović, P. Propylene epoxidation using molecular oxygen over copper- and silver- based catalysts: a review. *ACS Catal.* **10**, 13415–13436 (2020).
2. Herzberger, J. et al. Polymerization of ethylene oxide, propylene oxide, and other alkylene oxides: synthesis, novel polymer architectures, and bioconjugation. *Chem. Rev.* **116**, 2170–2243 (2016).
3. Martín, C., Fiorani, G. & Kleij, A. W. Recent advances in the catalytic preparation of cyclic organic carbonates. *ACS Catal.* **5**, 1353–1370 (2015).
4. Khatib, S. J. & Oyama, S. T. Direct oxidation of propylene to propylene oxide with molecular oxygen: a review. *Catal. Rev.* **57**, 306–344 (2015).
5. Nijhuis, T. A., Makkee, M., Moulijn, J. A. & Weckhuysen, B. M. The production of propene oxide: catalytic processes and recent developments. *Ind. Eng. Chem. Res.* **45**, 3447–3459 (2006).
6. Karmadonova, I. E., Zudin, V. N., Kuznetsova, N. I., Kuzhetsova, L. I. & Bal'zhinimaev, B. S. Preparation of ethylbenzene and isopropylbenzene hydroperoxides in the N-hydroxyphthalimide–Fe(III) homogeneous catalytic system and use of solutions in the epoxidation of olefins. *Catal. Ind.* **12**, 216–225 (2020).
7. Buijink, J. K. F., Van Vlaanderen, J. J. M., Crocker, M. & Niele, F. G. M. Propylene epoxidation over titanium-on-silica catalyst-the heart of the SMPO process. *Catal. Today* **93-95**, 199–204 (2004).
8. Lei, Y. et al. Increased silver activity for direct propylene epoxidation via subnanometer size effects. *Science* **328**, 224–228 (2010).
9. Ghosh, S. et al. Selective oxidation of propylene to propylene oxide over silver-supported tungsten oxide nanostructure with molecular oxygen. *ACS Catal.* **4**, 2169–2174 (2014).
10. Hua, Q. et al. Crystal-plane-controlled selectivity of Cu$_2$O catalysts in propylene oxidation with molecular oxygen. *Angew. Chem. Int. Ed.* **53**, 4856–4861 (2014).
11. Xi, Z., Zhou, N., Sun, Y. & Li, K. Reaction-controlled phase-transfer catalysis for propylene epoxidation to propylene oxide. *Science* **292**, 1139–1141 (2001).
12. Gordon, C. P. et al. Efficient epoxidation over dinuclear sites in titanium silicalite-1. *Nature* **586**, 708–713 (2020).
13. Signorile, M. et al. Titanium defective sites in TS-1: structural insights by combining spectroscopy and simulation. *Angew. Chem. Int. Ed.* **59**, 18145–18150 (2020).
14. Jin, K. et al. Epoxidation of cyclooctene using water as the oxygen atom source at manganese oxide electrocatalysts. *J. Am. Chem. Soc.* **141**, 6413–6418 (2019).
15. Seh, Z. W. et al. Combining theory and experiment in electrocatalysis: insights into materials design. *Science* **355**, eaad4998 (2017).
16. Jirkovsky, J. S., Busch, M., Ahlberg, E., Panas, I. & Krtil, P. Switching on the electrocatalytic ethene epoxidation on nanocrystalline RuO$_2$. *J. Am. Chem. Soc.* **133**, 5882–5892 (2011).

17. Luna, P. D. et al. What would it take for renewably powered electrosynthesis to displace petrochemical processes? *Science* **364**, eaav3506 (2019).

18. Winiwarter, A. et al. CO as a probe molecule to study surface adsorbates during electrochemical oxidation of propene. *ChemElectroChem* **8**, 250–256 (2021).

19. Maria, B.-B., Teresa, Ł., Helmut, B. & Ulrich, M. Propene oxidation and hydrogenation on a porous platinum electrode in acidic solution. *J. Phys. Chem. B* **107**, 4793–4800 (2003).

20. Sun, Y. P., Qiu, O., Xu, W. L. & Scott, K. A study of the performance of a sparged packed bed electrode reactor for the direct electrochemical oxidation of propylene. *J. Electroanal. Chem.* **503**, 36–44 (2001).

21. Winiwarter, A. et al. Towards an atomistic understanding of electrocatalytic partial hydrocarbon oxidation: propene on palladium. *Energy Environ. Sci.* **12**, 1055–1067 (2019).

22. Pulido, A., Concepción, P., Boronat, M. & Corma, A. Aerobic epoxidation of propene over silver (111) and (100) facet catalysts. *J. Catal.* **292**, 138–147 (2012).

23. Zhao, B. & Wang, G.-C. Theoretical investigation of propylene epoxidation on Ag(111) by molecular oxygen: Na(K,Cl) effects. *J. Phys. Chem. C.* **123**, 17273–17282 (2019).

24. Holbrook, L. L. & Wise, H. Electrooxidation of olefins at a silver electrode. *J. Catal.* **38**, 294–298 (1975).

25. Chou, T.-C & Chang, J.-C. Anodic oxidation of propylene on a screen electrode. *Chem. Eng. Sci.* **35**, 1581–1590 (1980).

26. Nguyen, N. L., De Gironcoli, S. & Piccinin, S. Ag-Cu catalysts for ethylene epoxidation: selectivity and activity descriptors. *J. Chem. Phys.* **138**, 184707 (2013).

27. Christopher, P. & Linic, S. Engineering selectivity in heterogeneous catalysis: Ag nanowires as selective ethylene epoxidation. *J. Am. Chem. Soc.* **130**, 11264–11265 (2008).

28. Hsieh, M. S., Su, H. J., Hsieh, P. L., Chiang, Y. W. & Huang, M. H. Synthesis of Ag₃PO₄ crystals with tunable shapes for facet-dependent optical property, photocatalytic activity, and electrical conductivity examinations. *ACS Appl. Mater. Interfaces* **9**, 39086–39093 (2017).

29. Martin, D. J., Umezawa, N., Chen, X., Ye, J. & Tang, J. Facet engineered Ag₃PO₄ for efficient water photooxidation. *Energy Environ. Sci.* **6**, 3380–3386 (2013).

30. Wu, Y. A. et al. Facet-dependent active sites of a single Cu₂O particle photocatalyst for CO₂ reduction to methanol. *Nat. Energy* **4**, 957–968 (2019).

31. Bi, Y., Ouyang, S., Umezawa, N., Cao, J. & Ye, J. Facet effect of single-crystalline Ag₃PO₄ sub-microcrystals on photocatalytic properties. *J. Am. Chem. Soc.* **133**, 6490–6492 (2011).

32. Zhu, G. et al. Self-regulated route to ternary hybrid nanocrystals of Ag-Ag₂S-CdS with near-infrared photoluminescence and enhanced photothermal conversion. *Nanoscale* **6**, 11147–11156 (2014).

33. Li, T., Lin, O., Lu, Z., He, L. & Wang, X. Preparation and characterization of silver loaded montmorillonite modified with sulfur amino acid. *Appl. Surf. Sci.* **305**, 386–395 (2014).

34. Chowdari, B. V. R., Mok, K. F., Xie, J. M. & Gopalakrishnan, R. Spectroscopic and electrical studies of silver sulfophosphate glasses. *J. Non-Cryst. Solids* **160**, 73–81 (1993).

35. Linic, S. & Barteau, M. A. Formation of a stable surface oxametallacycle that produces ethylene oxide. *J. Am. Chem. Soc.* **124**, 310–317 (2002).

36. Liu, J.-C., Tang, Y., Chang, C.-R., Wang, Y.-G. & Li, J. Mechanistic insights into propene epoxidation with O₂-H₂O mixture on Au₇/α-Al₂O₃: a hydroproxyl pathway from ab initio molecular dynamics simulations. *ACS Catal.* **6**, 2525–2535 (2016).

37. Zhang, B. et al. High-valence metals improve oxygen evolution reaction performance by modulating 3d metal oxidation cycle energetics. *Nat. Catal.* **3**, 985–992 (2020).

38. Wang, Y.-X. & Wang, G.-C. A systematic theoretical study of water gas shift reaction on Cu(111) and Cu(110): potassium effect. *ACS Catal.* **9**, 2261–2274 (2019).

39. Jin, G. et al. In situ FT-IR study on the direct gas phase epoxidation of propylene over Ag-MoO₃ catalyst. *Acta Phys. Chim. Sin.* **22**, 809–814 (2006).

40. Huang, W. X. & White, J. M. Transition from π-Bonded to di-σ metallacyclic propene on O-modified Ag(111). *Langmuir* **18**, 9622–9624 (2002).

41. Xiong, W. et al. Fine cubic Cu₂O nanocrystals as highly selective catalyst for propylene epoxidation with molecular oxygen. *Nat. Commun.* **12**, 5921 (2021).

42. Liu, Z.-P. & Hu, P. General rules for predicting where a catalytic reaction should occur on metal surfaces: a density functional theory study of C-H and C-O bond breaking/making on flat, stepped, and kinked metal surfaces. *J. Am. Chem. Soc.* **125**, 1958–1967 (2003).

43. Medford, A. J. et al. From the sabatier principle to a predictive theory of transition-metal heterogeneous catalysis. *J. Catal.* **328**, 36–42 (2015).

44. Zhou, Y. et al. Dopant-induced electron localization drives CO₂ reduction to C₂ hydrocarbons. *Nat. Chem.* **10**, 974–980 (2018).

45. Huang, H. et al. Understanding of strain effects in the electrochemical reduction of CO₂: using Pd nanostructures as an ideal platform. *Angew. Chem. Int. Ed.* **56**, 3594–3598 (2017).

46. Zhang, S., Kang, P. & Meyer, T. J. Nanostructured tin catalysts for selective electrochemical reduction of carbon dioxide to formate. *J. Am. Chem. Soc.* **136**, 1734–1737 (2014).

47. Lum, Y. et al. Tuning OH binding energy enables selective electrochemical oxidation of ethylene to ethylene glycol. *Nat. Catal.* **3**, 14–22 (2020).

48. Geng, Z. et al. Oxygen vacancies in ZnO nanosheets enhance CO₂ electrochemical reduction to CO. *Angew. Chem. Int. Ed.* **57**, 6054–6059 (2018).

49. Kresse, G. & Furthmüller, J. Efficiency of ab-initio total energy calculations for metals and semiconductors using a plane-wave basis set. *Comput. Mater. Sci.* **6**, 15–50 (1996).

50. Perdew, J. P., Burke, K. & Ernzerhof, M. Generalized gradient approximation made simple. *Phys. Rev. Lett.* **77**, 3865–3868 (1996).

51. Kresse, G. & Joubert, D. From ultrasoft pseudopotentials to the projector augmented-wave method. *Phys. Rev. B* **59**, 1758–1775 (1999).

52. Henkelman, G., Uberuaga, B. P. & Jónsson, H. A climbing image nudged elastic band method for finding saddle points and minimum energy paths. *J. Chem. Phys.* **113**, 9901–9904 (2000).

53. Nørskov, J. K. et al. Origin of the overpotential for oxygen reduction at a fuel-cell cathode. *J. Phys. Chem. B* **108**, 17886–17892 (2004).

Author contributions

Z.G. supervised this project. J.K and M.C. performed most of the experiments and analyzed the experimental data. J.-K.Z. carried out DFT calculations and analyzed the computational data. J.K., M.C., X.K., and W.Z. conducted XANES measurements and analyzed the results. M.W., Q.C., and C.L. provided help in materials synthesis and characterizations. J.K., Z.G., and J.Z. wrote the manuscript. All authors discussed the results and assisted during manuscript preparation.

Competing interests

The authors declare no competing interests.

Additional information

Supplementary information The online version contains supplementary material available at https://doi.org/10.1038/s41467-022-28516-0.

Correspondence and requests for materials should be addressed to Zhigang Geng.

Peer review information *Nature Communications* thanks the anonymous reviewer(s) for their contribution to the peer review of this work.

Reprints and permission information is available at http://www.nature.com/reprints

Publisher's note Springer Nature remains neutral with regard to jurisdictional claims in published maps and institutional affiliations.